Bull. Mater. Sci. (2025) 48:108
https://doi.org/10.1007/s12034-025-03458-7

Comparative analysis of corrosion resistance in Ni-, Cu- and Co-based alloys in synthetic mine water

SILAS I HANGO[1,2,*], LESLEY A CORNISH[1] and LESLEY H CHOWN[1]

[1]School of Chemical and Metallurgical Engineering, DSI-NRF Centre of Excellence in Strong Materials and African Materials Science and Engineering Network, University of the Witwatersrand, Wits, Johannesburg 2050, South Africa
[2]Department of Mechanical and Metallurgical Engineering, University of Namibia, Ongwediva 15006, Namibia
*Author for correspondence (shango@unam.na)

MS received 16 January 2025; accepted 13 May 2025

Abstract. To address the corrosion of mild steel in aggressive mine water environments, nickel-chromium-iron (Hastelloy® G30), copper-nickel-tin (ToughMet® 3), and cobalt-chromium-tungsten (Stellite® 6B) alloys were evaluated for their corrosion resistance. The study examined their behaviour in synthetic mine water at pH levels 6, 3 and 1 using potentiodynamic polarisation, alongside microstructural, hardness, and X-ray diffraction (XRD) analyses. Hastelloy® G30 had equiaxed γ grains with Cr_3C_2 precipitates, ToughMet® 3 displayed large, irregular grains, and Stellite® 6B showed γ grains with Cr_3C_2 at boundaries and twinning. Hastelloy® G30 and Stellite® 6B demonstrated active-passive transitions with localized corrosion, while ToughMet® 3 showed pseudo-passivation with severe pitting across all pH levels. Hastelloy® G30 achieved the lowest corrosion rates at pH 6 (0.63 ± 0.01 μm·y^{-1}) and pH 3 (0.74 ± 0.05 μm·y^{-1}) but performed poorly at pH 1 (7.75 ± 0.64 μm·y^{-1}), with a hardness of 180 ± 10 HV_2. Stellite® 6B had low corrosion rates at pH 3 (1.32 ± 0.34 μm·y^{-1}) and pH 1 (5.61 ± 1.13 μm·y^{-1}), with a hardness of 368 ± 13 HV_2. ToughMet® 3 showed high corrosion rates, particularly at pH 1 (118.78 ± 8.00 μm·y^{-1}). Stellite® 6B is the most promising alternative for harsh mining environments, offering optimal hardness and corrosion resistance.

Keywords. Hard alloys; corrosion resistance; potentiodynamic polarization; passivation; mine water corrosion.

1. Introduction

Mine water corrosion significantly impacts the underground infrastructure, causing material degradation, higher maintenance costs, and environmental risks. Understanding its electrochemical behaviour is crucial for developing effective mitigation strategies and enhancing the longevity of mining equipments and their structures. In various mines, mild steel shaft sleeves, valves and casings play a crucial role in water pump systems. These systems operate continuously to extract water from underground reservoirs, preventing mine flooding. However, these components undergo substantial degradation due to the combined effects of corrosion from mine water and wear caused by the mechanical interaction with solid particles suspended in water [1]. Many underground mines contain extensive sulphide deposits. For instance, a copper mine might possess a high copper concentration (∼1.6 wt%) along with zinc, lead, silver and gold as by-products [2–4]. These mines also contain alkaline earth elements, rare earth elements, sulphates, nitrates, and have an acidic pH, which can vary seasonally. Additionally, they exhibit high electrical conductivity and total dissolved solids. Seepages from the tailings dump, consisting of pyrite (FeS_2), react with oxygen, nitrogen, water vapour, chlorine and other gases, making the mine water acidic and corrosive [3]. This acidic and corrosive mine water frequently causes corrosion and breakdown of pumping systems, resulting in frequent maintenance, downtime, and part replacement that is deemed unacceptable.

To mitigate corrosion in mine pumping systems, candidate hard alloys such as a nickel-based alloy (Ni–Cr–Fe, Hastelloy® G30), copper-based alloy (Cu–Ni–Sn, ToughMet® 3) and a cobalt-based alloy (Co–Cr–W, Stellite® 6B) were selected as a replacement material for the failing steel pump components due to their hardness and corrosion resistance properties. The corrosion behaviour of these hard alloys have received extensive research attention, particularly in reducing and oxidising environments. While some researchers have explored the impact of corrosion on hard metals, emphasising corrosion resistance and hardness; there has been limited research on the electrochemical responses of nickel-, copper- and cobalt-based hard alloys in mine water, despite their extensive use in mining and metallurgical applications. These alloys are often exposed to aggressive environments containing sulphate, chloride and other corrosive species, which can significantly impact their passivation behaviour and long-term stability.

Published online: 29 August 2025

Understanding their electrochemical responses under different pH conditions is important for improving their corrosion resistance and optimising their performance in harsh mining environments.

Hastelloy® G30 is a highly corrosion resistant nickel-chromium-iron based superalloy, especially against corrosion in phosphoric acid or chloride-induced localized attack such as hydrochloric, sulphuric and nitric acids [5]. Corrosion behaviour of Hastelloy alloys offer superior performance similar to stainless steel grades, however, the alloys have low hardness (160–230 HV_2) with active-passivation behaviour in many solutions [6–9]. The high chromium content promotes the formation of a protective Cr_2O_3 film, preventing nickel ions or electrons migration towards the surface, enhancing corrosion resistance [6,10]. Pitiya *et al* [4] and Guo *et al* [6] found that apart from this compact inner Cr_2O_3 passive film, there is also a loose outer layer consisting of iron oxide (Fe_2O_3) or nickel iron oxide ($NiFe_2O_4$).

ToughMet® 3 is a Cu–Ni–Sn superalloy with good tensile strength, high hardness and minimum corrosion resistance in acidic environment, where it experiences localized corrosion deterioration such as pitting corrosion, hydrogen embrittlement and fatigue corrosion [11,12]. Due to its good strength and elastic behaviour, the alloy is mostly used for bearing, sleeve and other high-strength wear-resistant parts, high performance engines as well as mining, industrial and heavy equipment due to its ability to resist mechanical wear [11,13].

Copper-based alloys in natural sea water undergo dealloying and intergranular corrosion due to bacterial sulphide attack on nickel in grain boundaries, accelerating corrosion [14]. Additionally, Hamidah *et al* [15] concluded that electrolyte ion attacks lead to a reduction in the strength of the internal structure of copper alloys, rendering them more susceptible to fatigue. This may lead to failure of an engineering material. In most acidic media, copper-based alloys experience passive and pseudo-passivation behaviour due to corrosion product of Cu_2O or $Cu_2Cl(OH)_3$) [15].

The Stellite® 6B alloy is extensively used in various industrial applications to protect mild steel components. These applications include safeguarding slurry pump elements such as casings, sleeves, and valves, as well as being used in physiological orthopedic implants like artificial knees and hips. This widespread adoption is primarily due to its commendable mechanical properties and exceptional corrosion resistance [16]. Moreover, Stellite® 6B alloys are widely utilized across diverse sectors for applications such as cutting tools and hard-facing castings. These include, but are not limited to, power generation, steel manufacturing, chemical processing, oil and gas, and marine environments [17]. Comprising mainly cobalt (Co), with chromium (Cr) added to fortify the Co matrix and facilitate the formation of chromium carbides (Cr_3C_7 or $Cr_{23}C_6$), these alloys also develop a protective passive film of chromium oxide (Cr_2O_3). Additionally, tungsten (W) is incorporated to enhance hardness [18,19]. The alloy spontaneously passivates in various environments, which is observed during anodic potentiodynamic polarization measurements [20,21].

Thus, this study aimed to systematically investigate and compare the microstructural, hardness, and electrochemical behaviour of Hastelloy® G30, ToughMet® 3, and Stellite® 6B hard alloys. Optical microscopy and scanning electron microscopy (SEM) were utilized to analyse and determine the microstructural features and elemental compositions of these alloys. The phases present in the alloys were identified through X-ray diffraction (XRD) analysis. The potentiodynamic polarization technique was employed to examine and compare the passivation behaviour and corrosion mechanisms of the alloys in synthetic mine water at varying pH levels of 6, 3 and 1. The best-performing alloy was identified as a potential replacement for corroding mild steel in acidic mine environments, where material selection is crucial for ensuring durability and long-term performance.

2. Materials and experimental methods

2.1 *Materials*

The materials studied were nickel-chromium-iron (Hastelloy® G30, UNS N06030), copper-nickel-tin (ToughMet® 3, UNS C72800), and cobalt-chromium-tungsten (Stellite® 6B, UNS R30006) hard alloys, supplied as bars by Multi Alloys, South Africa. Their nominal compositions are given in Table 1. These alloys were selected for their exceptional corrosion resistance in both acidic and alkaline environments, along with their commendable hardness values [22–27].

2.2 *Microstructures and X-ray diffraction characterization*

The bulk samples underwent a comprehensive preparation regimen involving cutting, hot mounting in resins, and subsequent wet grinding with silicon carbide papers ranging from 80 to 1200 grit, followed by polishing using diamond suspensions of 9, 6, 3 and 1 μm, to achieve a thorough analysis of their surface characteristics. Cleanliness was ensured by rinsing with de-ionized water and degreasing with acetone. Subsequently, Carl Zeiss Sigma field emission scanning electron microscopy coupled with energy dispersive X-ray spectroscopy (SEM-EDX) was employed for the detailed observation and analysis of the bulk alloy microstructures. Grain size and carbide proportions within the Stellite® 6B bulk alloy were quantified using the line intercept method on micrographs captured at a magnification of 1000x, with a minimum of 20 measurements conducted at various points. Furthermore, phase identification in all the alloys was facilitated by a Bruker D2 Phaser®

Table 1. Chemical compositions of the tested hard alloys (in wt%) [5,11,59].

Hard alloy	Co	Cu	Ni	Cr	Mo	W	Mn	Fe	Si	C	Nb	Sn
Hastelloy® G30 [5]	5.0	2.0	Bal.	30.0	5.5	2.5	1.5	15.0	0.8	0.03	0.8	—
ToughMet® 3 [11]	—	Bal.	15	—	—	—	—	—	—	—	—	8
Stellite® 6B [59]	Bal.	—	2.6	28.8	1.5	4.5	1.0	2.5	1.3	1.2	—	—

diffractometer, with Fe filtered Co-Kα radiation and analysed via Panalytical Highscore Plus analytical software.

2.3 *Hardness tests*

The Hastelloy® G30, ToughMet® 3 and Stellite® 6B bulk alloys were prepared metallographically as previously described (see section 2.2). Vickers hardness measurements were done on polished surfaces using a Vickers FM-700 hardness tester, with each sample subjected to a dwell time of 10 s and seven repetitions to ensure reproducibility, employing a load of 2 kg (HV_2).

2.4 *Electrochemical measurements*

The corrosion resistance of the samples was evaluated in synthetic mine water, the composition of which is detailed in table 2 [1]. The solution was prepared by dissolving analytical-grade salts in deionized water to establish a baseline pH of 6, and subsequently acidified to pH levels of 3 and 1 using 32% HCl. Deionized water was used to eliminate interfering ions, ensuring consistent and reproducible corrosion testing. All experiments were conducted at 22.3 ± 1.0°C.

The experimental setup for the electrochemical measurements were conducted in a 500 mL three-electrode cell, with the samples acting as the working electrode, a saturated calomel electrode (SCE) as the reference electrode in a Luggin capillary to minimize the ohmic drop errors and a graphite counter electrode. Samples were prepared by cold-mounting in epoxy resin after being connected to a copper wire with aluminum conducting tape. Subsequently, they underwent wet grinding with silicon carbide papers, rinsing with de-ionized water, ethanol degreasing, and air drying. Each sample had an exposed area of 1 cm^2 to the corrosive environment.

Table 2. Chemical composition of synthetic mine water for corrosion testing [1].

Salt	Concentration ($mg \cdot L^{-1}$)
$MgSO_4$	198
Na_2SO_4	1215
$CaCl_2$	1038
NaCl	1379

Before scanning, samples were immersed for an hour to stabilize the open circuit potential (OCP). Extreme pH conditions (pH 6 and pH 1) were selected for clearer contrast in corrosion behaviour. Potentiodynamic polarisation measurements were performed from –750 to 1200 mV *vs.* the reference electrode potential at a scan rate of 0.2 $mV \cdot s^{-1}$ using an Auto Tafel potentiostat with Auto Tafel (V1.79 and Auto LPR V2.7h) software. The chosen potential range covers both the active corrosion and passivation regions, allowing for the identification of key parameters such as corrosion potential, passivation behaviour, pitting potentials, and current densities. Duplicate tests were performed to ensure reproducibility. Corrosion rates were calculated using equation (1) [28] through Tafel extrapolation of the potentiodynamic polarization curves, enabling the extraction of corrosion current densities from the corresponding Tafel slopes. Following polarization, optical and scanning electron microscopy, XRD analysis were also conducted to examine surface morphologies and films.

$$\text{Corrosion rate}\left(\frac{\mu m}{y}\right) = \mathrm{K} \cdot \frac{E_w}{\rho} \cdot i_{corr} \quad (1)$$

where K is the conversion factor (= 0.00327), E_w is the equivalent weight in g, ρ is the density of the material in $g \cdot cm^{-2}$ and i_{corr} the corrosion current density in $\mu A \cdot cm^{-2}$.

3. Results and discussion

3.1 *Microstructural and X-ray diffraction analyses*

Figure 1 shows the SEM microstructures of the bulk alloys before corrosion tests. Hastelloy® G30 (figure 1a) composed of light grey network and dark grey matrix phases, consisting of irregular to approximately equiaxed shape γ (i.e., a Ni-rich solid solution with Cr) grains with twinning, which were more visible in the optical microstructure (figure 1b). The average grain size of the Hastelloy® G30 was 256.1 ± 15.2 μm. Apart from γ-Ni, Cr_3C_2 was also confirmed by XRD in Hastelloy® G30 alloy (figure 2a). The carbides detected by XRD (figure 2a), likely fine dispersions formed at grain boundaries [29,30], make it difficult

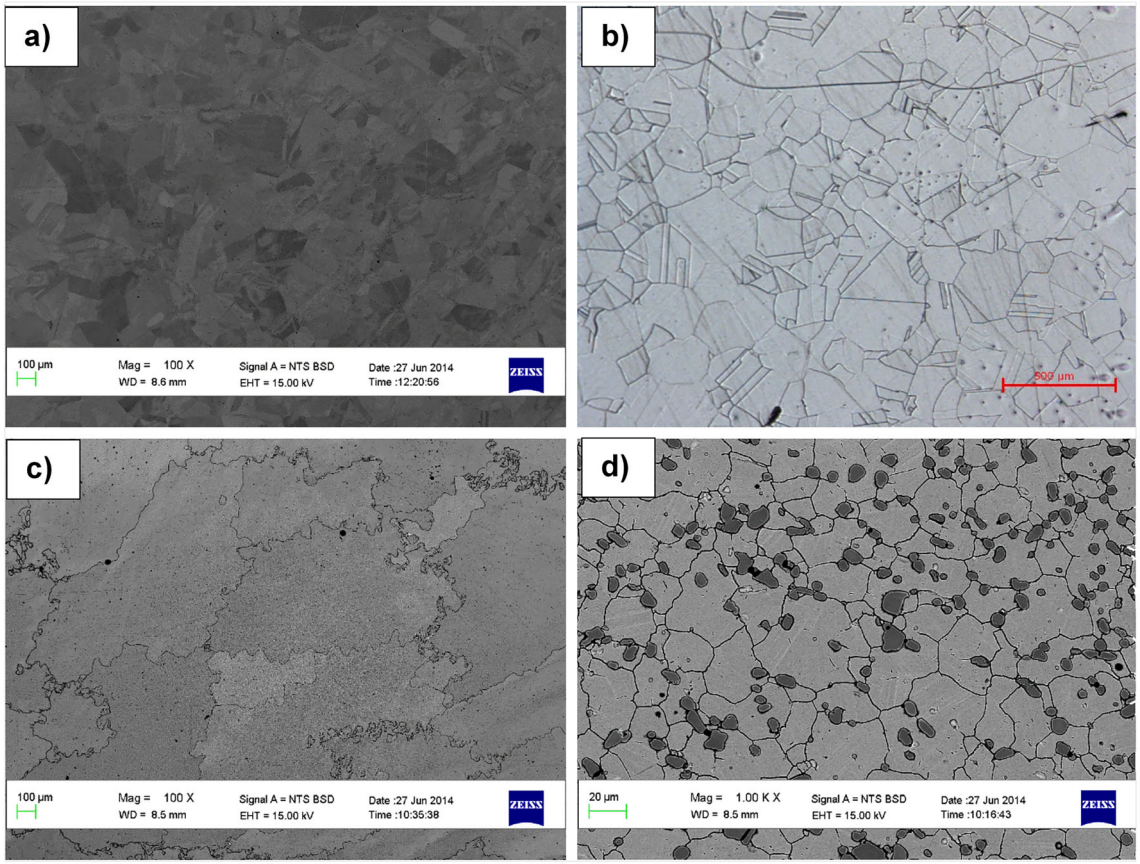

Figure 1. SEM-BSE micrographs of (**a**) Hastelloy® G30 and (**b**) optical micrograph Hastelloy® G30, showing twins in the light and dark grey grains, (**c**) SEM-BSE micrographs of ToughMet® 3, showing large grains and (**d**) SEM-BSE micrographs of Stellite® 6B alloys displaying twins and carbides distributed within the matrix and along the grain boundaries [28].

for them to observe in microstructure analyses (figure 1a and b). ToughMet® 3 (figure 1c) showed large and irregular grains, more prominently visible at lower magnifications, comprised with an average grain size of 722.3 ± 53.4 µm. Only peaks from Cu-based solid solution were detected (figure 2b). Stellite® 6B (figure 1d) is comprised of well-defined γ (i.e., a cobalt-rich solid solution with Cr), also exhibiting twinning and also large Cr_3C_2 precipitated at the grain boundaries, confirmed by XRD (figure 2c).

Hastelloy® G30 and Stellite® 6B alloys exhibited a polycrystalline structure characterized by γ matrices and carbides, whereas ToughMet® 3 alloy displayed a single-phase structure, each possessing inherent properties influenced by grain sizes and carbide distribution (excluding ToughMet® 3). The samples were not subjected to heat treatment for microstructure optimisation, although such a treatment could potentially enhance their properties. Any microstructure optimisation would be reserved for future investigations. Decreasing grain sizes typically leads to increased hardness, but there is a concern regarding reduced corrosion resistance due to the greater grain boundary area, as grain boundaries are typically prone to corrosion initially [28].

A more uniform distribution of carbides could also prove beneficial, particularly for Stellite® 6B (figure 1d), which exhibited relatively large carbides at grain boundaries and within grains, and for Hastelloy® G30, where carbides were exclusively present within grains. The large grain sizes observed in ToughMet® 3 may result from the segregation of Cu–Ni–Sn alloy during solidification, driven by significant differences in the melting points of the constituent elements. This segregation enhances the mechanical properties of the alloy [13].

The SEM-EDX data for the bulk alloys is outlined in table 3. Hastelloy® G30 predominantly featured Ni, Cr and Fe as major constituents, supplemented by minor elements including Mo, W, Co, Cu, Mn, Si and Al. Meanwhile, ToughMet® 3 exhibited single-phase grains containing Cu, Ni and Sn. EDX analyses of the Stellite® 6B alloy indicated minimal variations in composition across all phases (Table 3), revealing Co and Cr as the primary constituents, with minor quantities of W, Fe, Ni and Mn. Stellite® 6B had a larger grain size (381.4 ± 13.6 µm). The carbide fraction for Stellite® 6B was 16 ± 1.5% while the precipitates for Hastelloy® G30 may be formed as thin films along grain boundaries, which were too small to measure, and this is

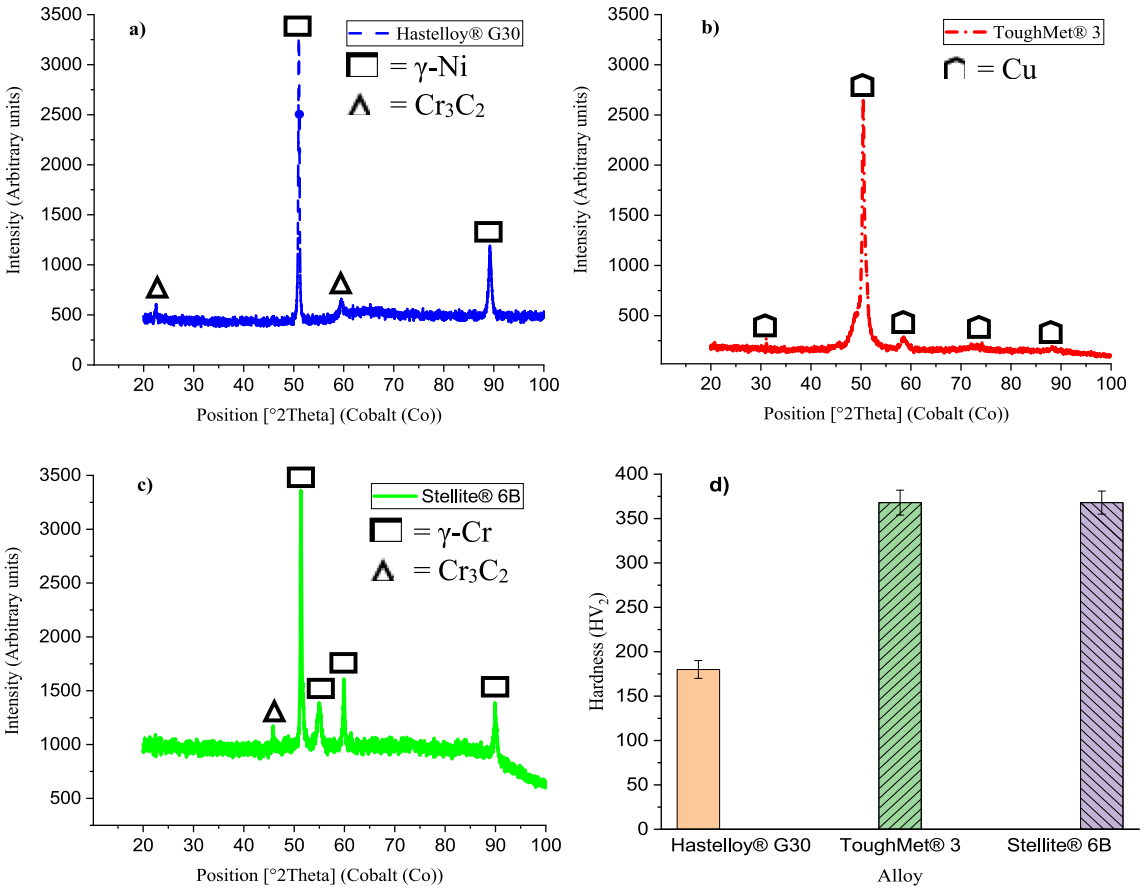

Figure 2. XRD patterns of (**a**) Hastelloy® G30 alloy with γ-Ni and Cr_3C_2 phases, (**b**) ToughMet® 3 alloy with Cu solid solution only, and (**c**) Stellite® 6B showing γ-Co and Cr_3C_2 phases before corrosion testing. Microhardness of the alloys is in (**d**), showing ToughMet® 3 and Stellite® 6B equally harder than the Hastelloy® G30.

Table 3. SEM-EDX phase analyses of the Hastelloy® G30, ToughMet® 3 and Stellite® 6B hard alloys (figure 1) before corrosion testing.

Element (wt%)	Hastelloy® G30			ToughMet® 3		Stellite® 6B		
	Overall	Light grey	Dark grey	Overall	Grains	Overall	Light grey	Dark grey
Cu	1.7 ± 0.3	2.3 ± 0.2	2.4 ± 0.2	78.3 ± 0.2	76.7 ± 1.0	—	—	—
Al	0.2 ± 0.0	0.3 ± 0.1	—	—	—	—	—	—
Ni	41.8 ± 0.5	44.8 ± 0.1	44.8 ± 0.3	13.9 ± 0.1	14.9 ± 1.0	1.7 ± 0.1	2.1 ± 0.1	—
Si	0.6 ± 01	0.1 ± 0.0	0.2 ± 0.0	—	—	0.4 ± 0.0	0.5 ± 0.0	—
Cr	29.8 ± 0.2	28.8 ± 0.2	28.9 ± 0.1	—	—	29.5 ± 1.0	24.0 ± 0.1	75.3 ± 0.3
Co	2.7 ± 0.1	2.3 ± 0.1	2.4 ± 0.3	—	—	46.2 ± 0.4	53.7 ± 0.1	9.3 ± 0.1
Fe	15.3 ± 0.4	12.8 ± 0.0	12.9 ± 0.1	—	—	1.7 ± 0.1	1.9 ± 0.1	0.6 ± 0.0
Mo	3.5 ± 0.3	5.4 ± 0.1	5.3 ± 0.3	—	—	—	0.7 ± 0.4	—
Mn	1.3 ± 0.0	1.1 ± 0.1	1.0 ± 0.1	—	—	1.5 ± 0.1	1.6 ± 0.2	1.3 ± 0.1
W	3.3 ± 0.1	2.1 ± 0.1	2.3 ± 0.1	—	—	4.8 ± 0.2	5.2 ± 0.2	3.1 ± 0.4
Sn	—	—	—	7.8 ± 0.1	8.4 ± 0.4	—	—	—
O	—	—	—	—	—	7.4 ± 1.0	6.5 ± 0.3	7.4 ± 1.0
C	—	—	—	—	—	7.6 ± 1.1	3.9 ± 1.0	10.6 ± 0.2

where the Cr_3C_2 (figure 2a) is suspected to be. Stellite® 6B had 7.7 ± 0.1 wt% O and 0.4 ± 0.0 wt% Si for the matrix. Carbon was found in the dark phase, with 10.5 ± 0.2 wt% (figure 1d).

3.2 *Hardness of the alloys*

Microhardness measurement results are presented in (figure 2d). Hastelloy® G30 had a lowest hardness (180 ± 10 HV_2) while ToughMet® 3 (368 ± 14 HV_2) and Stellite® 6B (368 ± 13 HV_2) had equally high hardness. The high hardness of ToughMet® 3 probably resulted from spinodal hardening, where nanoscale phase separation enhances strength without brittleness [31]. Solid solution strengthening would also contribute, as Ni and Sn atoms could distort the copper lattice, hindering dislocation movement [29,32]. The high hardness of Stellite® 6B was likely attributed to the combined effects of finer grains and the presence of Cr_3C_2 carbides, figures 1d and 2c, which are added specifically to enhance wear resistance and improve wear properties [33].

The hardness of the alloys (figure 2d) is crucial in applications requiring wear resistance. The hardness values of ToughMet® and Stellite® 6B were comparable to those reported by Yu *et al* [13] and Bozzi *et al* [34] for Haynes 6B and 25 alloys (310–466 HV_2). However, other studies have reported significantly higher hardness values for various cobalt-based alloys. For instance, Ahmed *et al* [35] cited hardness ranging from 419–704 HV_2 for Stellite® 6 and 20, while Hango *et al* [17] quoted hardness of 368–547 HV_2 for Stellite® 6B and 6, while Krell *et al* [36] found Co–Cr–W–C alloys to have hardness in the range of 360–620 HV_2, and lower hardness values of 230–390 HV_2 for Co–Cr–W/Mo–Ni/Fe–C alloys.

Although with very lower hardness (201–235 HV_2) than Stellite® 6B coatings, An *et al* [37] studied hardness evolution in cobalt alloys (200–280 HV_2), where hardness resulted from the formation of martensite and mechanical twins during cold rolling.

The higher C and W contents of Stellite® 6B than Hastelloy® G30 and ToughMet® 3 facilitated the formation of tungsten carbides [38,39], while the low contents of Ni, Si and Mn support the formation of hard phases, resulting in an increased overall hardness [33]. The carbides were visible in the microstructures (figure 1), and were observed in the XRD patterns (figure 2).

3.3 *Corrosion of the hard alloys*

3.3a *Open circuit potential measurements:* Figure 3 illustrates the open circuit potential (OCP) measurements for Hastelloy® G30, ToughMet® 3, and Stellite® 6B bulk alloys in synthetic mine water at pH 6 and pH 1. The OCP results at pH 3 were omitted due to their transitional behaviour offering no distinct mechanistic insight beyond the trends already established at pH 6 and 1. The average OCP values for each alloy are summarized in table 4. The variation in OCP values at both pH levels followed a similar trend, with all alloys shifting towards more negative potentials. This shift was more pronounced at pH 6. During the first 30 min of immersion, the potential for all alloys dropped gradually, likely due to the initial passivation process [1,40,41]. The continued shift towards more noble potentials indicated progressive changes in the passive layers.

After one hour of immersion, the potentials of the alloys nearly stabilized. The results revealed that ToughMet® 3 and Stellite® 6B exhibited less negative potentials with decreasing pH compared to Hastelloy® G30 at both pH levels. However, Hastelloy® G30 exhibited a significant shift towards more negative values, suggesting greater resistance to corrosion at lower pH levels.

3.3b *Potentiodynamic polarization measurements:* The potentiodynamic polarisation curves of Hastelloy® G30, ToughMet® 3 and Stellite® 6B bulk alloys in synthetic mine water at pH 6, 3 and 1 at ambient temperature (22.3 ± 1.0°C) are presented in figure 4. The Hastelloy® G30 (figure 4a) and Stellite® 6B (figure 4b) bulk alloys exhibit the spontaneous passive behaviour without active–passive transition, at all pH values tested, suggesting the formation of stable and protective passive film was formed [17,20,42]. This behaviour is likely attributed to the presence of Cr, with the stability of the protective film specifically enhanced by Si and Mn [43]. The ToughMet® 3 (figure 4c) bulk alloy also experienced an active-passive and then pseudo-passive (unstable or apparent passivation) behaviour at all pH values tested.

Hastelloy® G30 and Stellite® 6B exhibited an extensive passivation range spanning approximately −350 mV to around 750 mV *vs.* SCE (figure 4). However, pitting occurred when the protective thin film was locally breached, resulting in elevated current densities at these corrosion potentials [44,45]. As the passive and transpassive regions of the polarization curves nearly coincided, the corrosion resistances of the Hastelloy® G30 and Stellite® 6B alloys appeared quite similar, despite notable differences in their microstructures (figure 1). The lower Mo content in Stellite® 6B compared to Hastelloy® G30, likely contributed to the more pronounced pitting corrosion observed in Stellite® 6B (figure 7e and f). ToughMet® 3 exhibited a limited passivity range, spanning approximately 0 mV to around 400 mV *vs.* SCE, followed by pitting. It demonstrated higher passive current densities across all pH values, indicating inferior corrosion resistance in the tested environment.

Table 5 presents the corrosion potentials (E_{corr}), current densities (i_{corr}), and corrosion rates of Hastelloy® G30, ToughMet® 3, and Stellite® 6B hard alloys in synthetic mine water at pH levels of 6, 3 and 1 as deduced from

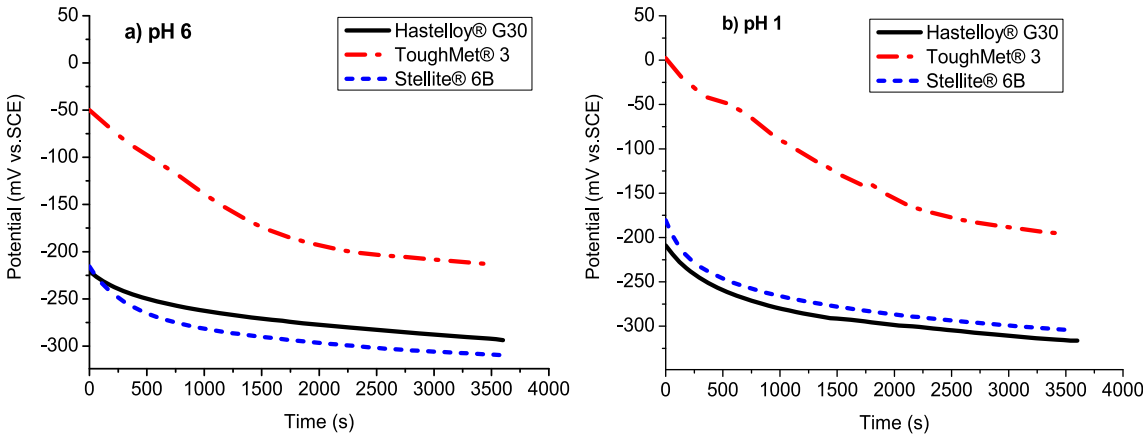

Figure 3. Variation of OCP over time for Hastelloy® G30, ToughMet® 3, and Stellite® 6B hard alloys in synthetic mine water at (**a**) pH 6 and (**b**) pH 1.

Table 4. Open circuit potential results of Hastelloy® G30, ToughMet® 3 and Stellite® 6B bulk alloys in synthetic mine water at pH levels of 6 and 1.

Bulk alloy	OCP (mV *vs.* SCE)	
	pH 6	pH 1
Hastelloy® G30	−177.5 ± 5.2	305.4 ± 6.1
ToughMet® 3	−160.4 ± 6.2	85.3 ± 4.6
Stellite® 6B	−190.8 ± 4.1	180 ± 3.2

corrosion results in figure 4. E_{corr} for Hastelloy® G30 changed to more negative values, i_{corr} changed with no trends and corrosion rate increased when the pH was decreased. E_{corr} for ToughMet® 3 changed from more to less negative values while i_{corr} and corrosion rate increased when the pH was decreased. The corrosion potential of Stellite® 6B became more negative at pH 3 but showed no clear trend. The corrosion current density remained the same at pH 6 and 3, but was higher at pH 1. Similarly, the corrosion rate varied without a clear trend as the pH decreased. It can be concluded that corrosion rate ($\mu m \cdot y^{-1}$) rankings at pH 6 was: ToughMet® 3 (73.93 ± 9.12) > Stellite® 6B (5.81 ± 0.33) > Hastelloy® G30 (0.63 ± 0.01), at pH 3: ToughMet® 3 (94.54 ± 6.11) > Stellite® 6B (1.32 ± 0.34) > Hastelloy® G30 (0.74 ± 0.05) and at pH 1: ToughMet® 3 (118.78 ± 8.00) > Hastelloy® G30 (7.75 ± 0.64) > Stellite® 6B (5.61 ± 1.13). On average, Stellite® 6B demostrated better corrosion resistance in the synthetic mine water than Hastelloy® G30 and ToughMet® 3 (figure 5).

Figure 4 also shows that Hastelloy® G30 and Stellite® 6B demonstrated evidence of the formation of protective oxide films, while ToughMet® 3 experienced a non-protective oxide film. Hastelloy® G30 exists as nickel oxide (NiO), Stellite® 6B as chromium oxide (Cr_2O_3) and ToughMet® 3 as copper oxide (Cu_2O or $Cu_2Cl(OH)_3$). The equations (1–16) describe the chemical reactions that take place during the oxide film formation for Hastelloy® G30 (1–4) [46], ToughMet® 3 (5–8) [26], Stellite® 6B (9–12) [47] and Cr_2O_3 film (13–16) [47].

At the early stage of immersion in a deaerated synthetic mine water solution, oxidation occurs, causing the metal solid to transform into metal ions (M^{n+}), where M represents Ni, Cu, Co, or Cr and n^+ is the oxidation state of the reaction (equations 2, 6, 10 and 14). This oxidation is supported by a cathodic reaction (equations 3, 7, 11 and 15) resulting in the formation of hydrogen gas (H_2), and no hydroxide ions (OH^-) are formed since the solution is acidic. The metal ions then react with the solution to form metal hydroxides $M(OH)_n$ (equations 2, 8, 12 and 6), which further dissociate to form metal oxides (MO) (equations 5, 9, 13 and 17). Apart from ToughMet® 3, Hastelloy® G30 and Stellite® 6B may form Cr_2O_3 films due to the high content of Cr in their compositions.

$$Ni\ (s) \rightleftharpoons Ni^{2+}(aq) + 2e^- \quad (2)$$

$$2H_2O(l) + 2e^- \rightleftharpoons H_2(g) \quad (3)$$

$$Ni^{2+}(aq) + 2H_2O(l) \rightleftharpoons Ni(OH)_2(aq) + 2H^+(aq) \quad (4)$$

$$Ni(OH)_2(aq) \rightleftharpoons NiO(s) + H_2O(l) \quad (5)$$

$$Cu\ (s) \rightleftharpoons Cu^{2+}(aq) + 2e^- \quad (6)$$

$$2H_2O(l) + 2e^- \rightleftharpoons H_2(g) \quad (7)$$

$$Cu^{2+}(aq) + 2H_2O(l) \rightleftharpoons Cu(OH)_2(aq) + 2H^+(aq) \quad (8)$$

$$Cu(OH)_2(aq) + Cu\ (s) \rightleftharpoons CuO(s) + 2H^+(aq) + 2e^- \quad (9)$$

$$Co\ (s) \rightleftharpoons Co^{2+}(aq) + 2e^- \quad (10)$$

$$2H_2O(l) + 2e^- \rightleftharpoons H_2(g) \quad (11)$$

$$Co^{2+}(aq) + 2H_2O(l) \rightleftharpoons Co(OH)_2(aq) + 2H^+(aq) \quad (12)$$

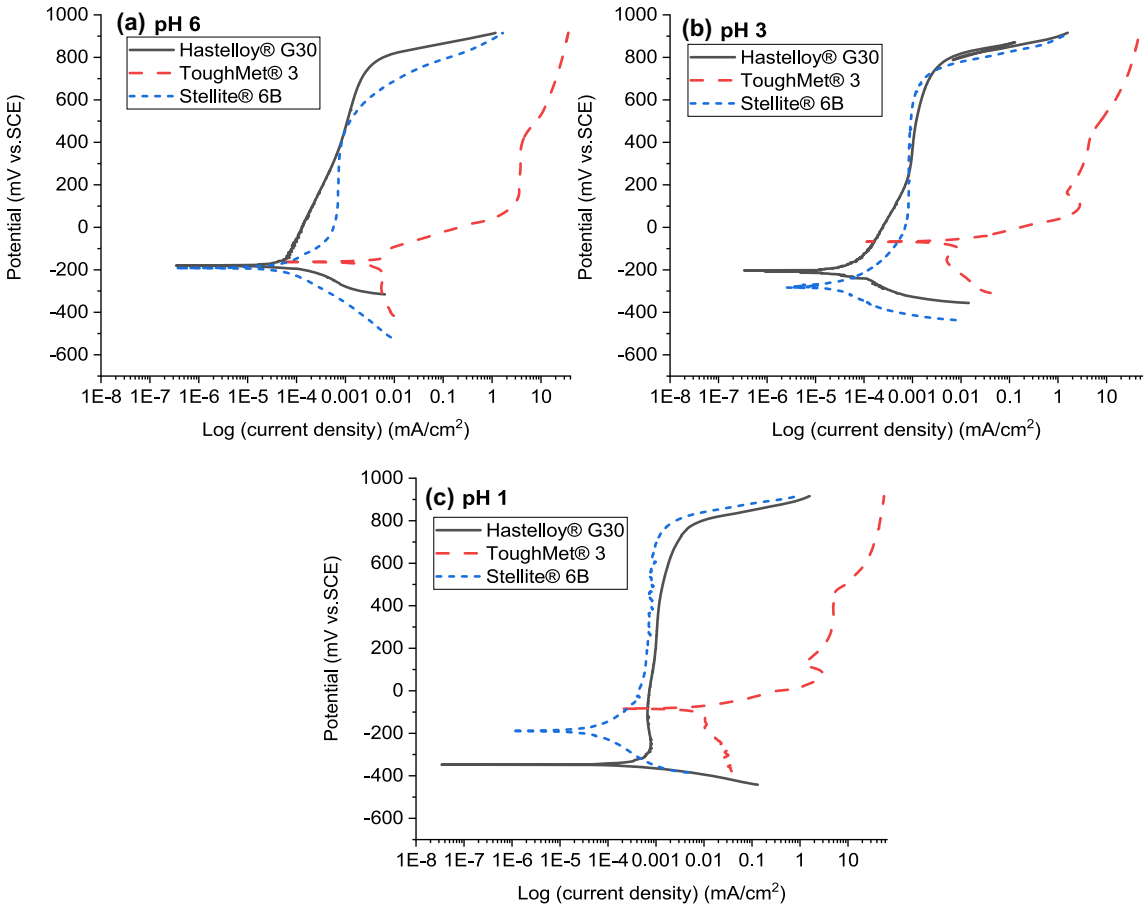

Figure 4. Potentiodynamic polarisation curves, showing the behaviour of Hastelloy® G30, ToughMet® 3, and Stellite® 6B hard alloys in synthetic mine water at (**a**) pH 6, (**b**) pH 3 and (**c**) pH 1.

Table 5. Potentiodynamic polarisation results of Hastelloy® G30, ToughMet® 3 and Stellite® 6B bulk alloys in synthetic mine water at pH level of 6, 3 and 1.

pH	Bulk alloy	E_{corr} (mV *vs.* SCE)	i_{corr} (μA·cm^{-2})	Corrosion rate (μm·y^{-1})
6	Hastelloy® G30	–179.4 ± 2.4	0.063 ± 0.001	0.63 ± 0.01
	ToughMet® 3	–162.5 ± 3.2	6.1 ± 0.4	73.93 ± 9.12
	Stellite® 6B	–191.7 ± 1.3	0.13 ± 0.02	5.81 ± 0.33
3	Hastelloy® G30	–202.2 ± 2.6	0.074 ± 0.00	0.74 ± 0.05
	ToughMet® 3	–67.2 ± 1.3	7.8 ± 0.6	94.54 ± 6.11
	Stellite® 6B	–283.2 ± 3.1	0.13 ± 0.04	1.32 ± 0.34
1	Hastelloy® G30	–347.1 ± 3.3	0.071 ± 0.001	7.75 ± 0.64
	ToughMet® 3	–83.9 ± 1.7	9.8 ± 0.7	118.78 ± 8.00
	Stellite® 6B	−182.8 ± 4.1	0.058 ± 0.004	5.61 ± 1.13

$$Co(OH)_2(aq) + Co\ (s) \rightleftharpoons CoO(s) + 2H^+(aq) + 2e^- \quad (13)$$

$$Cr\ (s) \rightleftharpoons Cr^{3+}(aq) + 3e^- \quad (14)$$

$$2H_2O(l) + 2e^- \rightleftharpoons H_2(g) \quad (15)$$

$$Cr^{3+}(aq) + 3H_2O(l) \rightleftharpoons Cr(OH)_3(aq) + 3H^+(aq) \quad (16)$$

$$Cr(OH)_3(aq) + Cr\ (s) \rightleftharpoons Cr_2O_3(s) + 3H^+(aq) + 3e^- \quad (17)$$

The passivation behaviour results showed that the Hastelloy® G30 and Stellite® 6B alloys were more

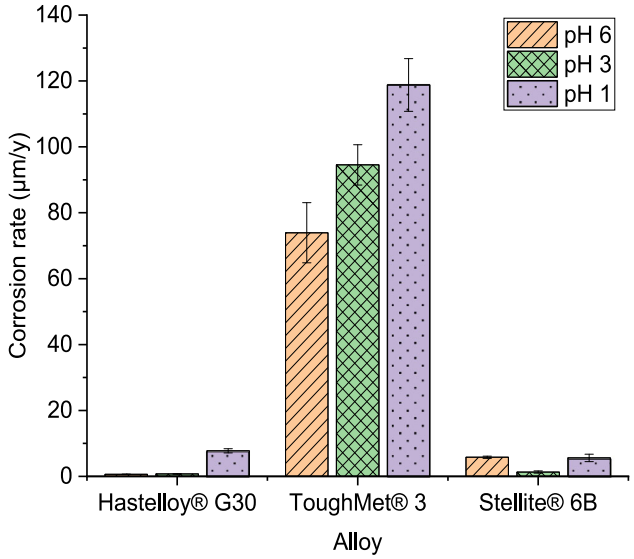

Figure 5. Corrosion rates of Hastelloy® G30, ToughMet® 3 and Stellite® 6B hard alloys in synthetic mine water at different pH levels.

stable than the ToughMet® 3 alloy at all pH values due to a thin oxide film formed on their surfaces, lowering the corrosion rate [6,39]. The corrosion rates of all samples, except for Stellite® 6B, were higher at pH 1 compared to pH 3 and 6 (figure 5), attributed to the higher chloride content in the solution [1], which has the potential to degrade the passivity.

The corrosion behaviour of the Stellite® 6B alloy was different, showing the lowest corrosion rate at pH 3, followed by pH 1 and pH 6 (figure 5). This indicates that a stable passive film could be formed on Stellite® 6B at pH 3 and 1 compared to pH 6, where the passive film was less effective [1,48]. The Stellite® 6B alloy exhibited both general and intergranular corrosion, evident from the presence of corrosion products and surface cracks along the grain boundaries (figure 7e and f) where intergranular corrosion also occurred. This suggests a strong correlation between grain boundary attack and crack initiation.

Figure 7e and f also show that the grain boundaries were more susceptible to corrosion [49]. Marimuthu and Kannoorpatti [50] found that carbides decomposed during sulphidation and within a cobalt-based clad layer, leading to severe corrosion along grain boundaries. However, this occurred at higher temperatures (800°C) and under sulphur partial pressures (10^{-8} and 10^{-10} atm) compared to the conditions in this investigation i.e. ambient temperature 22.3 ± 1.0°C. The carbides served as anodes to the matrix and were preferentially attacked [51,52]. Stellite® 6B has 1.0 wt% C (table 1) making it possible for the formation of Cr_3C_2, confirmed by XRD (figure 2).

At high pH levels, protective films likely formed, hinder the diffusion of hydrogen ions (figure 4). In contrast, lower pH levels led to the disruption of these films due to hydrogen evolution, thereby exposing the metal to the surrounding solution. This exposure heightened oxygen depolarization and hydrogen evolution, consequently elevating corrosion rates [53]. Additionally, the presence of increased chloride and sulphate ions in the solution further augmented the corrosion rate by enhancing the conductivity of the test solution and promoting the breakdown of protective films, which increases the corrosion rate. These ions are known to degrade passive layers (as depicted around ~750 mV *vs.* SCE in figure 4), and accelerate corrosion and expedite corrosion [41,54].

The wide range of spontaneous passivation behaviour (ranging from –150 to 750 mV *vs.* SCE) observed at pH 3, except for ToughMet® 3, was linked to the development of protective thin films consisting of Cr_2O_3 on the surface under low pH conditions [44,55–57]. This behaviour exhibited greater stability at pH 1 (ranging from approximately 150 to 900 mV *vs.* SCE), with pitting potentials falling between 670 and 900 mV *vs.* SCE, as evidenced by deep pits observed through SEM analysis (figure 7).

The corrosion mechanisms differed notably between Hastelloy® G30 and Stellite® 6B hard alloys compared to ToughMet® 3. However, the corrosion rates of Hastelloy® G30 were considerably lower than those of Stellite® 6B (table 5 and figure 5) at pH 6 and 3, but higher at pH 1. However, Hastelloy® G30 was susceptible to pitting corrosion (figure 7) and was less hard (figure 2). On the other hand, Stellite® 6B displayed superior hardness and corrosion rates, making it a promising alternative to mild steel in various industrial applications, including slurry pump components such as casings, sleeves, and valves [1,16,58].

3.3c *Microscopic morphologies of the alloys after corrosion tests:* The optical microscopic morphologies of the alloys exposed in synthetic mine water at different pH values are displayed in figure 6, and differentiated by colour observation. There were a little significant differences observed in the morphologies of the alloys when the pH was lowered. This means that the corrosion mechanism of the alloys at all pH values may be the same. For the Hastelloy® G30 (figure 6a–c), the surface was simply darkish with some white products. ToughMet® 3 (figure 6d–f) had little bluish green corrosion products of the surface at pH 6, and covered entirely with blackish to whitish at pH 3, and bluish green and white corrosion products at pH 1. The corrosion products on top of the Stellite® 6B (figure 6g-i) alloy showed brownish and whitish particles at all pH values, with greyish particles at pH 6.

Under SEM-secondary electron (SE) detector, the surface morphologies of the alloys after corrosion tests is synthetic mine water at pH 6 and 1 are shown in figure 7. Hastelloy® G30 alloy showed almost even surfaces with shallow and a few deep pits, which were more at pH 1 than pH 6 (figure 7a and b). ToughMet® 3 exhibited pitting and selective corrosion, resulting in a thick surface layer (figure 7c and d). Stellite® 6B, on the other hand, primarily underwent

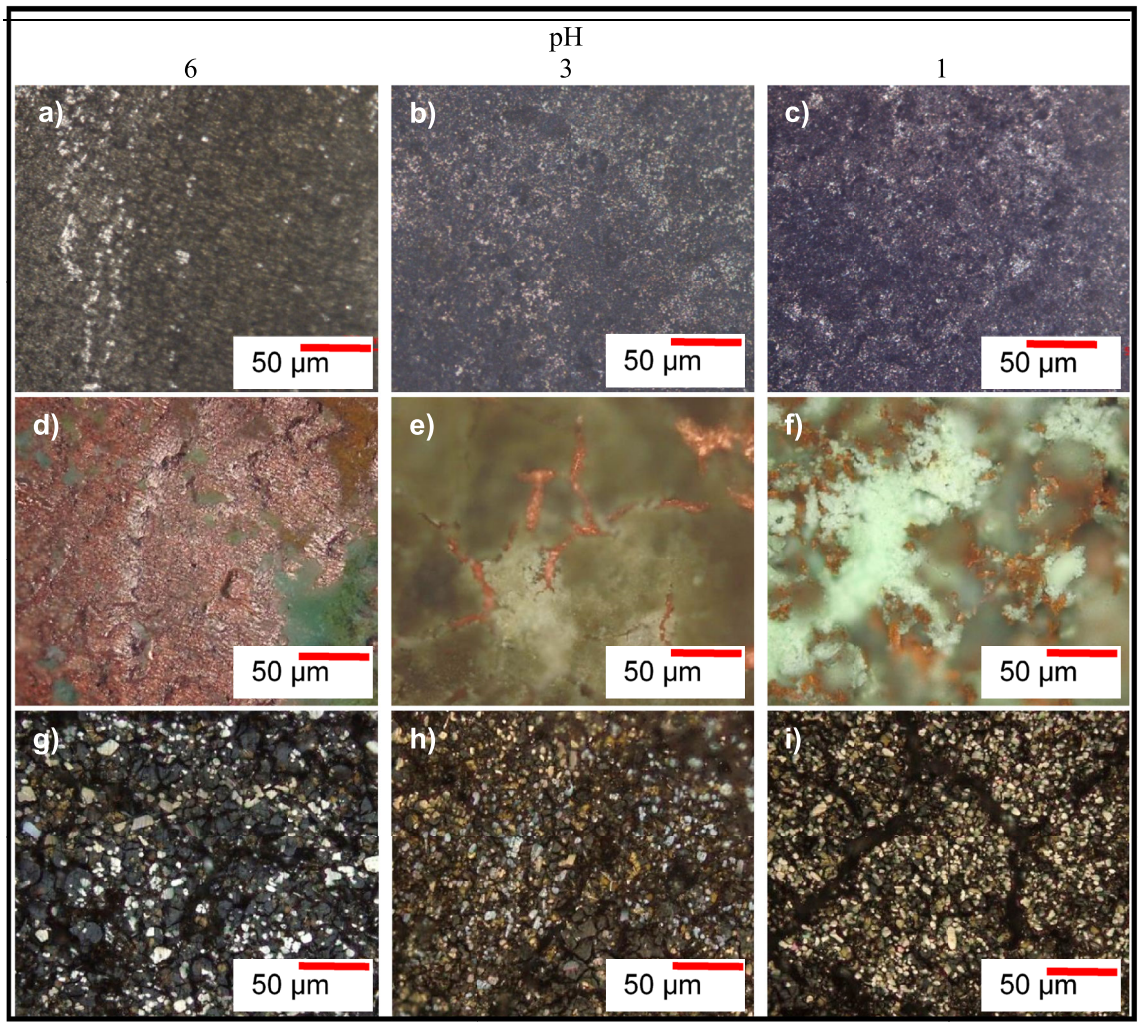

Figure 6. Optical micrographs (20X magnification) show (**a–c**) Hastelloy® G30, (**d–f**) ToughMet® 3, and (**g–i**) Stellite® 6B hard alloys following potentiodynamic polarisation in synthetic mine water with pH levels of 6, 3 and 1.

uniform corrosion, with instances of intergranular corrosion and small pits where carbides were removed, along with surface oxides as corrosion byproducts (figure 7e and f), observed across all pH levels.

3.3d *Corrosion products by XRD analyses:* To confirm the compositions of the corrosion products, SEM-EDX (table 6) and XRD (figure 8) analyses were used. XRD results showed that Hastelloy® G30 had Ni, Cr_2O_3 and $NiFe_2O_4$ after corrosion tests in all pH values (figure 8a).

EDX analysis conducted on the surface of figure 7c showed that ToughMet® 3 exhibited relatively high concentrations of Cu, O and Cl, but no detectable Sn (table 6) at any pH level. Comparing the data from tables 3 and 6, it was evident that the content of Cu and Sn decreased after corrosion. This suggests that Cu and Sn were preferentially removed from the sample, leaving behind Ni, which likely interacted with Cl and O from the solution. The phase compositions of the corrosion products, confirmed by XRD (figure 8b), consisted of Cu, along with a double-layered reaction product: copper (I) oxide (Cu_2O) beneath and a copper chloride hydroxide ($Cu_2Cl(OH)_3$) layer formed by the presence of chloride-containing electrolyte. For the Stellite® 6B alloy, the overall EDX analysis indicated elevated concentrations of Co, Cr, C, O and W on the surface across all pH levels (table 6). The increased concentration of O suggests the formation of a chromium oxide (Cr_2O_3) oxide film on the surface, a finding corroborated by XRD analysis (figure 8c).

To determine the most suitable alloy, both corrosion rates and hardness were evaluated. Hastelloy® G30 exhibited the lowest corrosion rates at pH 6 and 3 among the tested alloys; however, it was significantly less hard than ToughMet® 3 and Stellite® 6B. Conversely, ToughMet® 3 displayed the highest corrosion rates compared to Hastelloy® G30 and Stellite® 6B. On average, Stellite® 6B demonstrated superior corrosion resistance across all pH values (table 5 and figure 5) while also exhibiting high

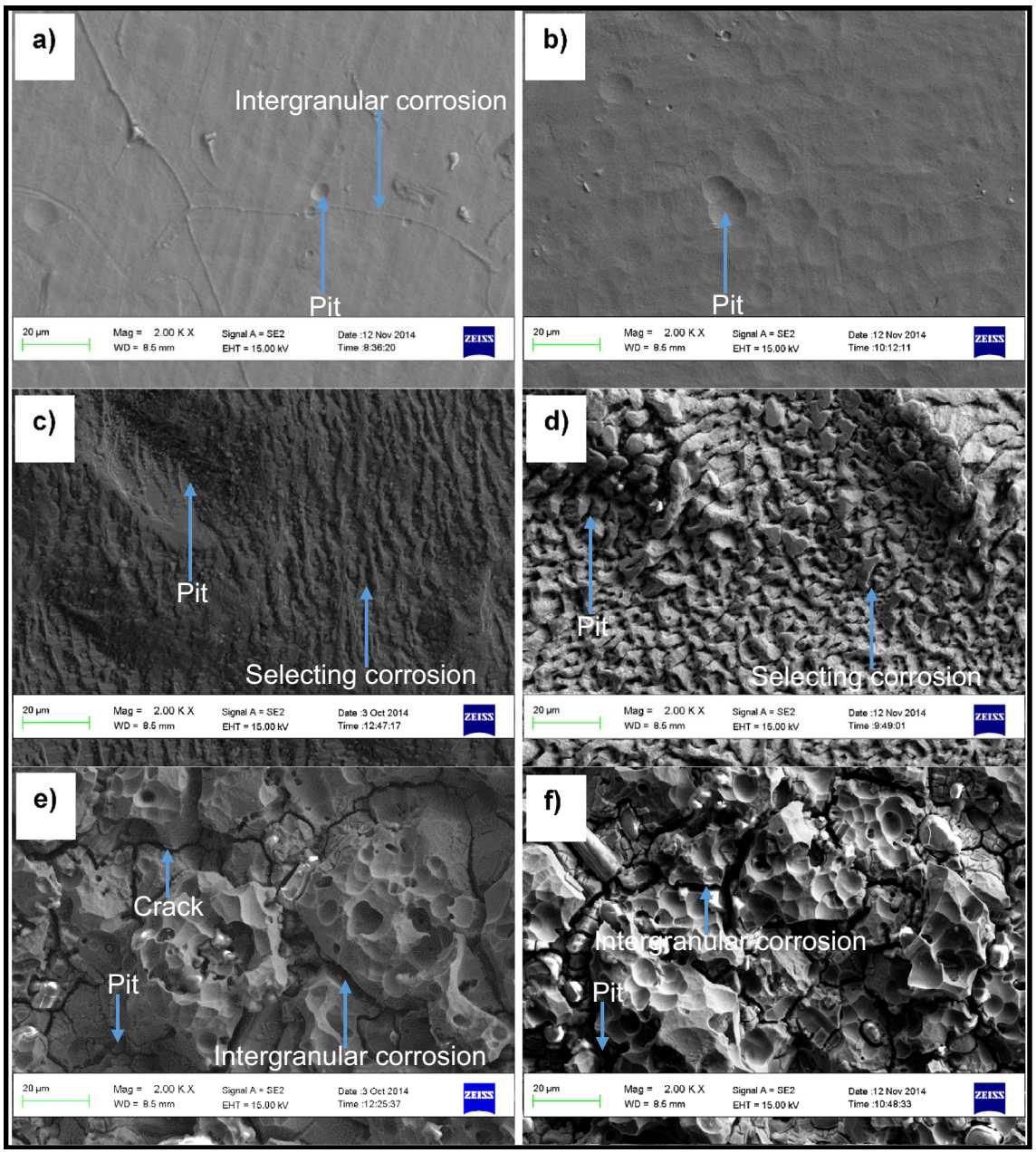

Figure 7. SEM-SE micrographs of the alloys after potentiodynamic polarisation in synthetic mine water at pH 6 and 1 (**a**) and (**b**) Hastelloy® G30, (**c**) and (**d**) ToughMet® 3 and (**e**) and (**f**) Stellite® 6B [28].

hardness (figure 2b). Although Hastelloy® G30 had lower hardness, the hardness for Stellite® 6B was comparable to that of ToughMet® 3. Due to its excellent combination of corrosion resistance and hardness, Stellite® 6B is a strong candidate for replacing mild steel in applications subjected to both corrosion and wear.

The limitation of this study was the lack of investigation into the corrosion behaviour of Ni-, Cu- and Co-based alloys in real mine water environments, which could have offered valuable insights into actual corrosion mechanisms. Also, electrochemical impedance spectroscopy (EIS) will be performed to gain insights into the corrosion mechanisms of the samples in the test solutions and to analyse their behaviour. Furthermore, other surface characterisation techniques, such as laser Raman spectroscopy (LRS) or X-ray photoelectron spectroscopy (XPS), should be used to accurately characterize the nature of the corrosion products formed after the tests. For future research, it is recommended to test these alloys in actual mine water conditions to validate the applicability of the findings in practical mining environments and to include EIS, LRS and/or XPS for a more comprehensive analysis.

Table 6. SEM-EDX surface analyses of the ToughMet® 3 and Stellite® 6B hard alloys (figure 7) after corrosion testing.

	pH 6		pH 3		pH 1	
Element (wt%)	ToughMet® 3	Stellite® 6B	ToughMet® 3	Stellite® 6B	ToughMet® 3	Stellite® 6B
C	—	14.6 ± 1.0	—	11.3 ± 1.0	—	6.6 ± 1.0
Ca	0.4 ± 0.0	0.3 ± 0.0	0.4 ± 0.0	0.2 ± 0.0	1.5 ± 1.0	0.2 ± 0.0
Cu	50.4 ± 7.0	—	64.4 ± 2.0	—	69.0 ± 12.0	—
O	11.3 ± 2.0	8.4 ± 0.3	12.9 ± 2.0	7.0 ± 0.1	12.4 ± 5.0	12.6 ± 0.2
Na	0.1 ± 0.0	0.3 ± 0.0	0.4 ± 1.0	0.2 ± 0.1	0.2 ± 0.0-	0.2 ± 0.0
S	0.4 ± 0.0	0.2 ± 0.0	0.2 ± 0.0	0.3 ± 0.0	0.3 ± 0.1-	0.8 ± 0.1
Cl	10.0 ± 3.0	—	20.3 ± 5.0	—	10.0 ± 5.0	—
Cr	—	26.6 ± 0.1	—	27.9 ± 0.3	—	29.6 ± 0.2
Mn	—	1.5 ± 0.0	—	1.7 ± 0.2	—	1.4 ± 0.1
Fe	—	1.9 ± 0.0	—	2.0 ± 0.0	—	1.5 ± 0.0
Co	—	38.8 ± 0.0	—	42.8 ± 1.0	—	35.8 ± 0.2
Ni	0.6 ± 0.0	—	0.2 ± 0.0	1.0 ± 0.1	0.9 ± 0.3	1.4 ± 0.0
Mo	—	—	—	5.5 ± 0.1	—	0.9 ± 0.4
W	—	6.1 ± 1.0	—	5.5 ± 0.1	—	8.7 ± 0.4

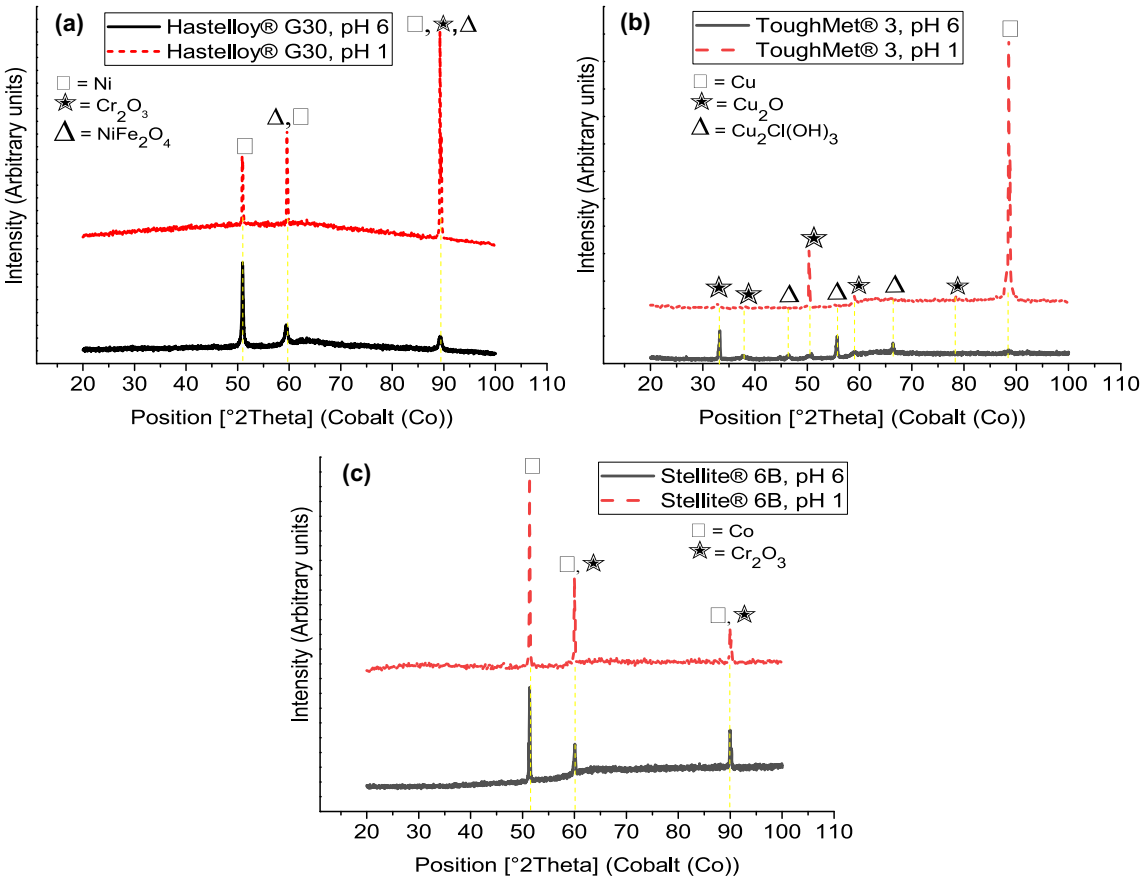

Figure 8. XRD patterns of the alloys after potentiodynamic polarisation in synthetic mine water at pH 6 and 1 (**a**) Hastelloy® G30, (**b**) ToughMet® 3 and (**c**) Stellite® 6B.

4. Conclusions

This study systematically investigated and compared the corrosion behaviour of Hastelloy® G30, ToughMet® 3, and Stellite® 6B hard alloys, aiming to identify a suitable replacement for corroding mild steel pump components in corrosive mine water environments. The microstructural characteristics, hardness, and corrosion resistance of these alloys were analysed, leading to the following key conclusions:

1. *Microstructure*:
   Hastelloy® G30 consisted of irregular and equiaxed γ-Ni grains with twinning and Cr_3C_2 precipitates. ToughMet® 3 exhibited large, irregular grains, while Stellite® 6B featured γ-Co grains with twinning and large Cr_3C_2 precipitates at the grain boundaries.
2. *Hardness determinants*:
   The presence of twins and Cr_3C_2 phases in Hastelloy® G30 and Stellite® 6B significantly influenced their hardness levels.
3. *Corrosion behaviour*:
   - Hastelloy® G30 and Stellite® 6B exhibited active-passive transition behaviour, forming protective thin films but experiencing pitting and intergranular corrosion.
   - ToughMet® 3 displayed pseudo-passivation, along with pitting and selective leaching corrosion in synthetic mine water at all tested pH values.
4. *Corrosion and hardness performance*:
   - Stellite® 6B had the lowest corrosion rate at pH 3 (1.32 ± 0.34 $\mu m \cdot y^{-1}$), followed by pH 1 (5.61 ± 1.13 $\mu m \cdot y^{-1}$) and pH 6 (5.81 ± 0.33 $\mu m \cdot y^{-1}$).
   - It also exhibited the highest hardness (368 ± 13 HV_2), comparable to ToughMet® 3 (368 ± 14 HV_2), and significantly higher than Hastelloy® G30 (180 ± 10 HV_2).
5. *Industrial application suitability*:
   Given its superior corrosion resistance and high hardness, Stellite® 6B is the most promising alloy for replacing mild steel in industrial applications, particularly in slurry pump components such as casings, sleeves and valves, where durability against corrosion and wear is critical.

Acknowledgments

We acknowledge the financial support received from the African Materials Science and Engineering Network (A Carnegie-IAS RISE network), as well as Multi Alloys, Midrand, South Africa, for the supply of the Hastelloy® G30, ToughMet® 3 and Stellite® 6B hard alloys and Mintek, Randburg, South Africa for corrosion experiments. We also express our heartfelt gratitude to Frank P L Kavishe and Josias W van der Merwe, who made significant contributions to this study before their passing. We honour their memory and acknowledge the profound impact they had on this research.

References

[1] Hango S I, Cornish L A, van der Merwe J W, Chown L H and Kavishe F P L 2024 *Results Mater.* **21** 100546
[2] *Central Operations Executive Summary* https://weatherlyplc.com (Accessed on 27 June 2023)
[3] Li H, Oraby E and Eksteen J 2022 *Miner. Eng.* **181** 107501
[4] Pitiya R, Jacob L and Emilinot R J 2022 *J. Mater. Sci. Chem. Eng.* **10** 1–14
[5] *Hastelloy® G-30® alloy: Principal features* www.haynesintl.com (Accessed on 27 June 2023)
[6] Guo C, Shi S, Dai H, Yu J and Chen X 2022 *Eng. Fail. Anal.* **140** 106580
[7] Chen L, Bai S L, Ge Y Y and Wang Q Y 2018 *Appl. Surf. Sci.* **456** 985–998
[8] Wang Q Y, Zhang X S, Zheng H B, Liu T Y, Dong L J, Zhang J *et al* 2023 *Appl. Surf. Sci.* **608** 155140
[9] Guo S, Xu D, Jiang G and Kuang W 2022 *J. Alloys Compd.* **907**
[10] Tang X, Wang S, Qian L, Li Y, Lin Z, Xu D and Zhang Y 2015 *Chem. Eng. Res. Des.* **100** 530–541
[11] *Tough solutions for tough applications* www.multialloys.co.za (Accessed on 27 April 2023)
[12] Loto T R 2022 *Mater. Today Proc.* **65** 2151–2155
[13] Yu Q X, Li X N, Wei K R, Li Z M, Zheng Y H, Li N J *et al* 2019 *Mater. Des.* **167** 107641
[14] Lu J C, Wang Z B, Hu H X and Zheng Y G 2024 *Corros. Sci.* **227**
[15] Hamidah I, Solehudin A, Hamdani A, Hasanah L, Khairurrijal K, Kurniawan T *et al* 2021 *Alexandria Eng. J.* **60** 2235–2243
[16] Prabhakaran D, Jegadeeswaran N, Somasundaram B and Raju B S 2020 *Mater. Today Proc.* **20** 173–176
[17] Hango S I, Cornish L A, Chown L H, van der Merwe J W and Kavishe F P L 2024 *Eng. Fail. Anal.* **155** 107717
[18] Mace A, Khullar P, Bouknight C and Gilbert J L 2022 *Dent. Mater.* **38** 1184–1193
[19] Wu Y, Schmitt T, Bousser E, Vernhes L, Khelfaoui F, Perez G *et al* 2020 *Surf. Coatings Technol.* **390** 125611
[20] Garcia-Falcon C M, Gil-Lopez T, Verdu-Vazquez A and Mirza-Rosca J C 2021 *Mater. Chem. Phys.* **260**
[21] Muangtong P, Rodchanarowan A, Chaysuwan D, Chanlek N and Goodall R 2020 *Corros. Sci.* **1**(172) 108740
[22] Zhu J, Ma L and Dwyer-Joyce R S 2020 *Wear* **460–461** 203474
[23] Rodriguez A A, Tylczak J and Ziomek-Moroz M 2018 *NACE - Int. Corros. Conf. Ser.* 2018-April 1–13
[24] Kamal K, Ding Y P, Liu R, Yao J H and Yao M X 2019 *J. Mater. Eng. Perform.* **28** 5605–5615
[25] Hong J H and Yeoh F Y 2019 *Mater. Today Proc.* **29** 196–201
[26] Su Y, Li L, Yin W, Chu G and Guan Y 2023 *Int. J. Electrochem. Sci.* **18** 100244

[27] Zhu Z, Li Y, Ma C, Liu X, Liu G, Wang S, Xu H and Zhang N 2021 *Corros. Sci.* **192**
[28] Williams D B and Butler E P 1981 *Int. Met. Rev.* **26** 153–180
[29] Sahu P, Pradhan S K and De M 2004 *J. Alloys Compd.* **377** 103–116
[30] Hango S I 2018 PhD Thesis (University of the Witwatersrand, Johannesburg, South Africa)
[31] Hogg J M, Miller J R, Pek M E, Carpenter M A and Stone H J 2025 *Mater. Sci. Eng. A* **930** 148144
[32] Guo Z, Jie J, Liu J, Yue S, Liu S and Li T 2020 *J. Alloys Compd.* **848** 156275
[33] Kevin P S, Tiwari A, Seman S, Mohamed S A B and Jayaganthan R 2020 *Coatings* **10** 1–17
[34] Bozzi A C, Ramos F D and Vargas D B O 2023 *Wear* **524–525** 204857
[35] Ahmed R, Lovelock H L de V and Davies S 2021 *Wear* **466–467** 203533
[36] Krell J, Röttger A and Theisen W 2020 *Wear* **444–445** 203138
[37] An X, Li Y, Ni S, Wang Z and Song M 2021 *Mater. Sci. Eng. A* **803** 1–9
[38] Jia L, Cui H, Yang S, Lv S, Xie X and Qu J 2023 *Prog. Nat. Sci. Mater. Int.* **33** 232–243
[39] Sedlaček M, Zupančič K, Šetina Batič B, Kosec B, Zorc M and Nagode A 2023 *Metals.* **13** 637
[40] Zamani P, Valefi Z and Jafarzadeh K 2022 *Ceram. Int.* **48** 1574–1588
[41] Hango S I, Cornish L A, van der Merwe J W and Chown L H 2024 *Int. J. Corros.* **2024**
[42] Al-Qawabah S, Mostafa A, Al-Rawajfeh A and Al-Qawabeha U 2020 *Mater. Tehnol.* **54** 785–790
[43] Zhang Y, Zhang X, Chen S, Liu J, Li T, Wang L and Wu K 2023 *Corros. Commun.* **9** 77–88
[44] Qin P, Chen L Y, Liu Y J, Zhao C H, Lu Y J, Sun H and Zhang L C 2023 *Corros. Sci.* **213** 110999
[45] Jeyaprakash N, Yang C H, Karuppasamy S S and Duraiselvam M 2023 *Trans. Indian Inst. Met.* **76** 491–503
[46] Jeyaprakash N, Yang C H, Karuppasamy S S and Dhineshkumar S R 2022 *Mater. Today Commun.* **31** 103370
[47] Long Y, Jiang W, Chen G, Luo J, Fan Y, Jin Q, Xie J, Feng Y and Xie J 2023 *Eng. Fail. Anal.* **148** 107198
[48] Zhang X, Li Y, Tang N, Onodera E and Chiba A 2014 *Electrochim. Acta* **125** 543–555
[49] Smolenska H 2010 *Solid State Phenom.* **165** 173–176
[50] Marimuthu V and Kannoorpatti K 2016 *J. Bio- Tribo-Corrosion* **2** 1–12
[51] Handoko W, Anurag A, Pahlevani F, Hossain R, Privat K and Sahajwalla V 2019 *Sci. Rep.* **9** 1–11
[52] Ahmed M, Talib N and Al-Gebory L 2020 *J. Inf. Sci. Eng.* **36** 217–229
[53] Cui Y, Qin Y, Dilimulati D and Wang Y 2019 *Int. J. Corros.* **2019** 1–11
[54] Guo S, Xu D, Li Y, Guo Y, Wang S and Macdonald D D 2021 *J. Supercrit. Fluids.* **1** 105138
[55] Zheng C, Liu Z, Liu Q, Li Y and Liu C 2022 *J. Mater. Res. Technol.* **18** 2194–2207
[56] Li W, Cao R, Xu L and Qiao L 2021 *Corros. Commun.* **4** 23–32
[57] Que Z, Ahonen M, Virkkunen I, Nevasmaa P and Rautala P 2022 *Nucl. Mater. Energy* **31** 101202
[58] *Wrought wear-resistant alloys* www.kennametal.com/stellite (Accessed on 27 June 2023)